

Sodium Vanadium Fluorophosphates (NVOPF) Array Cathode Designed for High-Rate Full Sodium Ion Storage Device

Dongliang Chao,* Chun-Han (Matt) Lai, Pei Liang, Qiulong Wei, Yue-Sheng Wang, Changrong (Rose) Zhu, Gang Deng, Vicky V. T. Doan-Nguyen, Jianyi Lin, Liqiang Mai, Hong Jin Fan, Bruce Dunn, and Ze Xiang Shen*

3D batteries continue to be of widespread interest for flexible energy storage where the 3D nanostructured cathode is the key component to achieve both high energy and power densities. While current work on flexible cathodes tends to emphasize the use of flexible scaffolds such as graphene and/or carbon nanotubes, this approach is often limited by poor electrical contact and structural stability. This communication presents a novel synthetic approach to form 3D array cathode for the first time, the single-crystalline $\text{Na}_3(\text{VO})_2(\text{PO}_4)_2\text{F}$ (NVOPF) by using VO_2 array as a seed layer. The NVOPF cathode exhibits both high-rate capability (charge/discharge in 60 s) and long-term durability (10,000 cycles at 50 C) for Na ion storage. Utilizing in situ X-ray diffraction and first principles calculations, the high-rate properties are correlated with the small volume change, 2D fast ion transport, and the array morphology. A novel all-array flexible Na^+ hybrid energy storage device based on pairing the intercalation-type NVOPF array cathode with a cogenetic pseudocapacitive VO_2 nanosheet array anode is demonstrated.

There is considerable interest in the development of new versatile and flexible power sources which meet the needs of next-generation shape-conformable and wearable electronics, including soft bendable mobile phones, roll-up displays, wearable sensors, and implantable medical devices.^[1–5] These energy-storage systems are generally based on lithium-ion and sodium-ion batteries (LIBs and SIBs), and flexible supercapacitors.^[6] One of the significant material-related challenges in this

field is to fabricate reliable electrodes that offer a combination of superior properties including mechanical flexibility, structural stability, and chemical stability to electrolytes in addition to high electron and ion conductivity.^[7] The integration of nano-sized active materials with a carbon-based scaffold, such as carbon nanotubes (CNTs), graphite, and graphene papers, has been demonstrated as one of the promising routes toward flexible batteries.^[8]

In research to date, the flexible batteries are largely based on 2D thin-film geometries. These configurations often suffer a compromise between the energy density and power density.^[1,9] In recent years there has been the realization that improved battery performance can be achieved by reconfiguring the electrode materials currently employed

in 2D geometry into 3D architectures, leading to a 3D architecture in which the various components (cathode, anode, and electrolyte) are arranged in either a periodic array or an aperiodic ensemble.^[1,8] A 3D matrix of electrode materials configured in an appropriate geometry should benefit the power requirement by shortening transport lengths, the energy density by enhancing loading per unit area, and the long-term cycling and bending conditions by stress release between the

Dr. D. Chao, Dr. C.-H. (Matt) Lai, Dr. Q. Wei, Prof. B. Dunn
Department of Materials Science and Engineering
University of California Los Angeles
CA 90095-1595, USA
E-mail: chaod@ntu.edu.sg

Dr. D. Chao, Dr. C. (Rose) Zhu, Prof. G. Deng, Prof. J. Lin, Prof. H. J. Fan, Prof. Z. X. Shen
School of Physical and Mathematical Sciences
Nanyang Technological University
Singapore 637371, Singapore
E-mail: zexiang@ntu.edu.sg

 The ORCID identification number(s) for the author(s) of this article can be found under <https://doi.org/10.1002/aenm.201800058>.

Prof. P. Liang
College of Optical and Electronic Technology
China Jiliang University
Hangzhou 310038, China

Dr. Q. Wei, Prof. L. Mai
State Key Laboratory of Advanced Technology for Materials Synthesis and Processing
Wuhan University of Technology
Wuhan 430070, China

Dr. Y.-S. Wang
Hydro-Québec's Research Institute
Varennes, Québec J3 × 1S1, Canada

Dr. V. V. T. Doan-Nguyen
Materials Research Laboratory
University of California
Santa Barbara, CA 93106, USA

DOI: 10.1002/aenm.201800058

arrays. Following this strategy, 3D arrays of various negative electrode materials such as ZnCo_2O_4 nanowires on carbon cloth,^[10] $\text{MoC}_{0.654}$ @carbon nanosheets on Ni foam,^[11] SnS and $\text{Li}_4\text{Ti}_5\text{O}_{12}$ nanosheets on graphene foam,^[12,13] have been successfully prepared. These 3D electrodes all show improved discharge capacities and rate capabilities compared to their planar counterparts. In contrast, the fabrication of LIB or SIB positive electrode materials (i.e., LiFePO_4 , LiCoO_2 , $\text{Na}_3\text{V}_2(\text{PO}_4)_3$ etc.) into a flexible 3D array architecture is rarely considered. The key challenges are related to the nucleation and oriented growth of cathode materials onto substrates, as well as the need to withstand high-temperature annealing in air. Xia et al.^[14] fabricated an LiCoO_2 nanowire array on an Au substrate using a Co_3O_4 precursor. While this approach circumvented the high-temperature annealing issue, the gold substrate is nonflexible, heavy, and expensive, which makes it less favorable and with limited energy density for practical applications.

In this communication, we use a two-step solvothermal method to fabricate oriented arrays of sodium vanadium fluorophosphate $\text{Na}_3(\text{VO})_2(\text{PO}_4)_2\text{F}$ (NVOPF) on a flexible, lightweight graphene foam backbone.^[15] This architecture enables high rate capability with long-term cycling performance. An all-array high-rate Na-ion energy storage device is assembled based on the NVOPF array positive electrode and a VO_2 negative electrode for the first time. This flexible all-vanadium-based^[16] energy storage device delivers energy and power densities as

high as 215 W h kg^{-1} and 5.2 kW kg^{-1} , respectively. By combining first principles computational methods and in situ X-ray diffraction (XRD), we attribute the charge storage properties of the NVOPF to the 3D array structure which has preferred crystallographic orientation along the (002) plane. These results provide insights regarding the design of nonplanar electrodes and their potential use in energy storage technology.

The synthesis of the 3D NVOPF array was achieved by a two-step solvothermal synthesis as illustrated in Figure 1A,B. In the first solvothermal step, seed layers of VO_2 nanosheets (NS) were deposited onto 3D graphene foam (GF) (Figure 1A). Then, during the second solvothermal step, the nanosheets transformed into an array of NVOPF rods (Figure 1B). The VO_2 nanosheets are mesoporous films, about 100 nm thick. XRD (as shown in Figure S1A, Supporting Information) is consistent with monoclinic VO_2 (B) films (JCPDS 31-1438) being deposited on the GF substrate (JCPDS 75-1621). High-resolution transmission electron microscopy (HRTEM) of the VO_2 NS in Figure 2B shows (200) planes with an interlayer spacing of 0.58 nm. The fast Fourier transform pattern of Figure 2B, shown in the inset, reveals the existence of (110) facets in the [002] zone axis, indicating that the layers of VO_2 are stacked along the [002] direction (see the geometrical model in Figure S1B, Supporting Information). This preferred crystal orientation of the VO_2 seed layer is critical for the subsequent growth of NVOPF along the [002] direction.

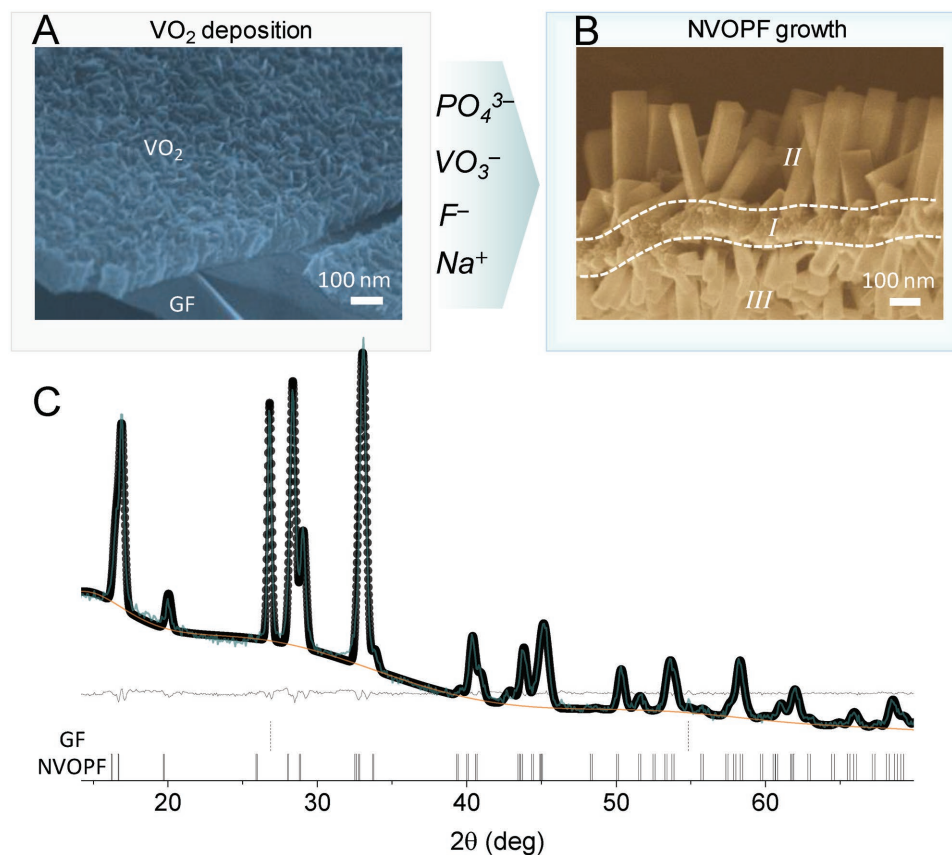


Figure 1. Synthesis strategy and microstructure of the GF supported NVOPF nanoarray. A,B) Cross-section FESEM images for the GF- VO_2 nanosheet seed layer precursor and GF-NVOPF array electrode. C) Rietveld refinement of the GF-NVOPF array electrode. Short dashes and the tick marks indicate the position of standard Bragg reflections from graphene foam and NVOPF, respectively. $R_p = 2.08\%$, $R_{wp} = 3.00\%$.

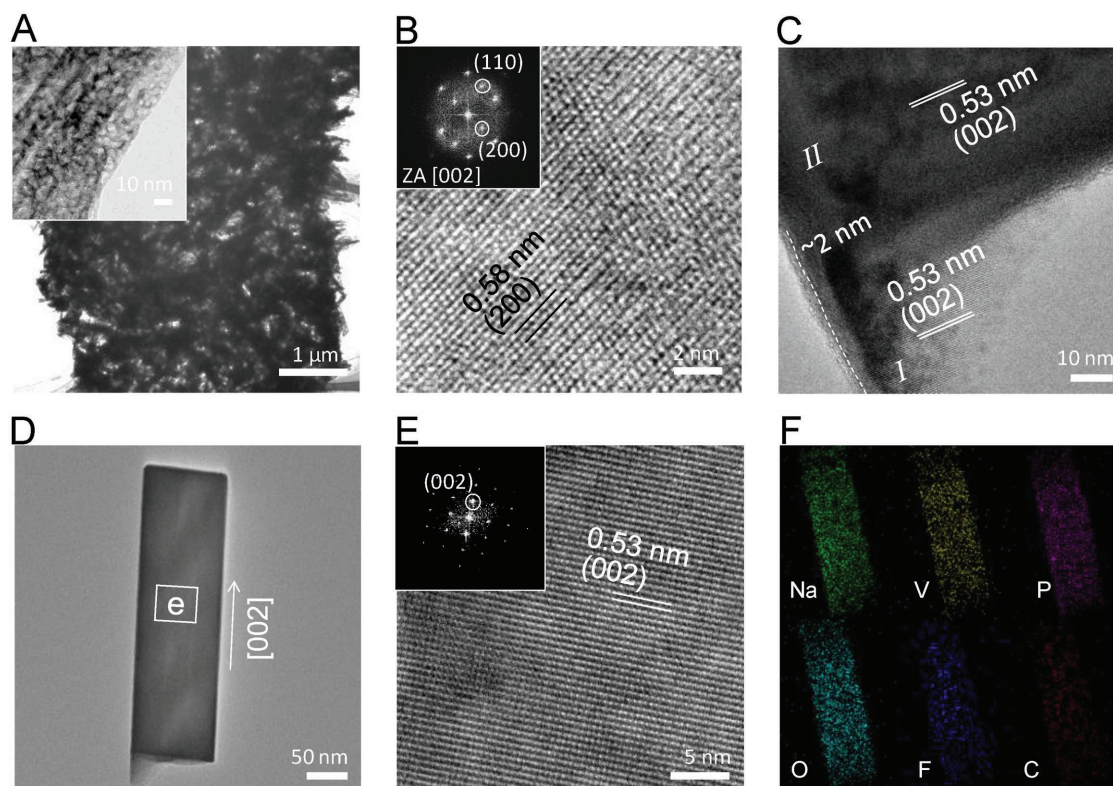


Figure 2. Structural characterization of the NVOPF nanostructures. A,B) TEM and HRTEM images of VO_2 nanosheets. Inset in panel (A): high-magnification TEM image. Inset in panel (B): The corresponding fast Fourier transform (FFT) pattern in the [002] zone axis. C) HRTEM image of the bottom part of the NVOPF nanorod showing interface between original VO_2 transformed NVOPF and epitaxially grown NVOPF rod. D,E) TEM and HRTEM images of the NVOPF nanorod. Inset in panel (E): Corresponding FFT pattern showing the single crystallinity. F) EDX elemental mappings of a single NVOPF nanorod.

In the second solvothermal reaction, a cuboid-shaped NVOPF array (Figure 1B) grew quasi-vertically on the hollow GF. The VO_2 NS provides the necessary seed layer for the growth of the NVOPF array (Figure S2, Supporting Information). The XRD in Figure 1C and Raman characterization (Figure S3, Supporting Information) indicate the presence of single-phase NVOPF without any VO_2 , suggesting that the VO_2 seed layer precursors were successfully transformed into NVOPF after the solvothermal reactions. The NVOPF nanorods which grow on both sides of GF are 80–100 nm in width and ≈ 400 nm in height (part II and III in Figure 1B). Their a and c parameters are 6.36 and 10.69 Å, respectively, and are consistent with reported work.^[17] This architecture is mechanically robust and enables electrolyte to penetrate to the redox-active NVOPF rods. Figure S4C,D (Supporting Information) shows that the NVOPF array electrode is flexible and foldable because of the GF scaffold. In addition, the growth of the NVOPF array nanostructures is also substrate friendly to carbon cloth (Figure S4F–H, Supporting Information). It is interesting to note that the GF/carbon cloth scaffolds have important synthetic contribution as they prevent undesirable aggregation and benefit for the array formation of the NVOPF freestanding electrode at the same time. Figure S5 (Supporting Information) discovers the morphologies of the NVOPF particles ($\approx 3 \mu\text{m}$) without the presence of a scaffold.

TEM images in Figure 2 provide details regarding the growth of the NVOPF rods. Figure 2C shows the interface between a single NVOPF rod (upper part of Figure 2C and also part II in Figure 1B) and its seed layer (lower part of Figure 2C and also part I in Figure 1B). This image indicates that the seed layer presents the same [002] preferred orientation as that of the NVOPF with the same spacing of 0.53 nm. It would seem, therefore, that during the synthesis, VO_2 NS was first converted to NVOPF after a 1 h solvothermal reaction (see Figure S6, Supporting Information). This was followed by epitaxial growth of the NVOPF rods along the [002] direction over the next 5 h of the solvothermal treatment. TEM and HRTEM images for the NVOPF nanorod in Figure 2D,E confirm the epitaxial growth of NVOPF along the [002] direction. Compared to the NVOPF particles, the anisotropic growth of NVOPF along the [002] direction improves fast Na ion insertion/extraction. Energy-dispersive X-ray (EDX) elemental mapping for a single rod in Figure 2F shows the elemental distribution of Na, V, O, P, F, and C. The carbon signals are introduced through a separate carbon annealing process which is discussed in the Experimental Section. This treatment produces ≈ 2 nm carbon-rich surface (Figure 2C) which increases the structural stability and electrical conductivity of the NVOPF rod. A density function theory (DFT) calculation of the VO_2 -NVOPF transition that leads to the formation of NVOPF is shown in Figure S7, Supporting Information and described in the Supporting Information. Taken together, these results establish

that a new synthesis route for growing epitaxial arrays of NVOPF on 3D graphene foams was successfully achieved.

In characterizing the electrochemical properties of NVOPF array electrodes, neither conductive additives nor binders nor a separate current collector were required as the material possessed sufficient ion and electron conduction to support the electrochemical reactions. The GF in the electrode serves as a foldable/compressible backbone for integrating the active materials, providing electron transfer, as well as functioning as a lightweight current collector. **Figure 3A** displays the galvanostatic profiles of the NVOPF array at rates from 0.5 to 60 C after an activation of 5 charge/discharge cycles (Figure S8A, Supporting Information), where 1 C is defined as 130 mA g^{-1} based on the theoretical capacity. Rate capabilities for the NVOPF array and a control electrode comprised of NVOPF particles are compared in **Figure 3B**. Both the NVOPF array and particle electrodes exhibit a discharge capacity of 130 mA h g^{-1} at a slow rate of 0.5 C, similar to that reported for NVOPF traditional slurry electrodes (Figure 3B; Figure S9, Supporting Information).^[18,19] However, the capacity is two times higher (80 mA h g^{-1} for array versus 34 mA h g^{-1} for the slurry) when the rate increases to 30 C. Furthermore, the discharge profiles and capacity (in Figure S10, Supporting Information) show negligible decay after folding the electrode twice. Electrochemical impedance spectroscopy (EIS) was used to characterize the charge transfer properties of the array and particle electrodes for the same area of 1 cm^2 . **Figure 3C** shows charge transfer resistance of the array is only 140Ω , whereas the resistance for the particle electrode increases to 375Ω . **Figure 3D** shows that

the GF-NVOPF array electrode exhibits very good long-term cycling stability, with only about a 10% decrease after 10 000 cycles at the high rate of 50 C. Indeed the scanning electron microscopy (SEM) examination of the electrode material after cycling in Figure S8B–D (Supporting Information) shows that the array architecture is well preserved without obvious deformation. The rate capability and cycling behavior of the NVOPF array electrode exceed that of other reported SIB cathodes shown in **Figure 3E** and Table S1 (Supporting Information). We believe that the array architecture with extensively exposed edges along the [002] direction is essential for achieving excellent electrochemical properties.

To complement the NVOPF positive electrode, we investigated the charge storage properties of VO_2 nanosheets anode for the first time which are deposited in the first solvothermal process. Over the potential range between 0.1 and 2.5 V, GF- VO_2 NS exhibited a highly reversible capability of 440 mA h g^{-1} at 200 mA g^{-1} and 300 mA h g^{-1} at 1500 mA g^{-1} (Figures S11A and S12, Supporting Information). Moreover, the GF- VO_2 NS electrode exhibits good cyclability with negligible capacity decay even after 500 cycles at 1500 mA g^{-1} . To understand the storage mechanism, the CV curves (in Figure S12, Supporting Information) are analyzed qualitatively by the power law relationship between current i and scan rate v ($i = av^b$, where a and b are both constants).^[12,20] The limiting values for b are 0.5 for a diffusion-controlled process and 1.0 for a capacitor-like process.^[21] The calculated b values for GF- VO_2 NS (in Figure S11B, Supporting Information) throughout most of the potential region is around 0.9 which decreases slightly below 1 V, suggesting

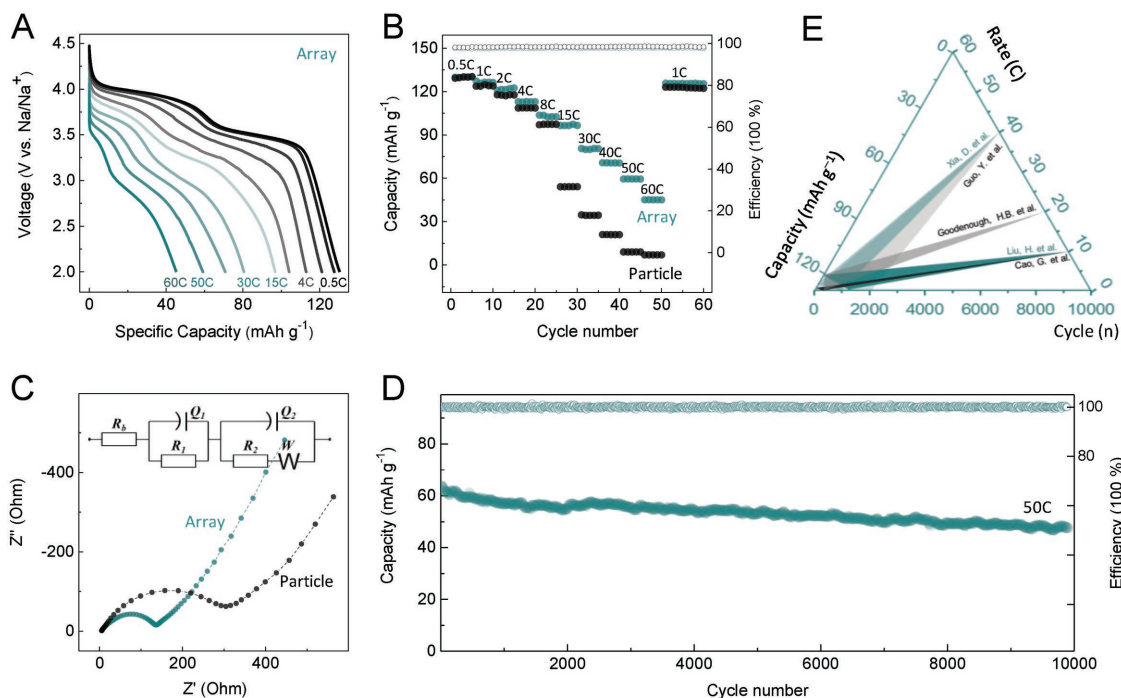


Figure 3. Na ion storage properties of the NVOPF array. A) Galvanostatic profiles of the NVOPF array electrode between 4.5 and 2.0 V after activation for 5 cycles. B) Rate performances of the NVOPF array and slurry electrodes at various current densities from 0.5 to 60 C. C) Electrochemical impedance spectroscopy of the NVOPF array and slurry electrodes at the fully charged state after activation for 5 cycles. The resistance is simulated using the equivalent circuit of $R_b(Q_1R_1)(Q_2(R_2W))$ shown in the inset. D) Long-term cycling performance of the NVOPF array electrodes at 50 C shows only a slight decrease in capacity. E) Comparison of the NVOPF array electrode with other reported sodium vanadium fluorophosphate materials.^[17–19,23,24]

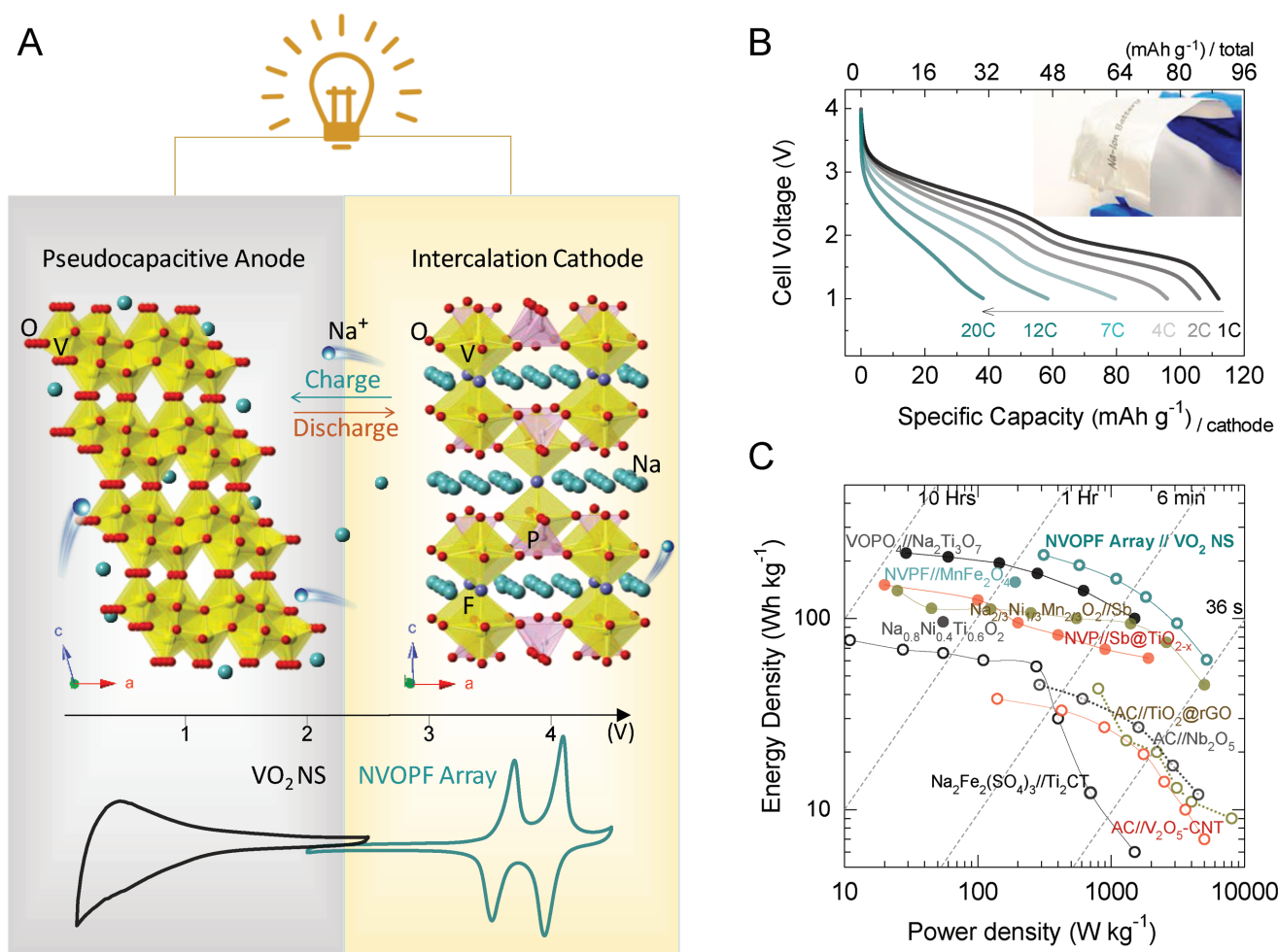


Figure 4. 3D flexible NVOPF array//VO₂ NS sodium ion hybrid device. A) Schematic illustration of the charge/discharge process (top) and the corresponding CV curves (bottom). B) Galvanostatic charge/discharge profiles from 1 to 20 C between 1 and 4 V (1 C is defined as 130 mA g⁻¹). Inset is the flexibility demonstration of assembled soft-packed pouch cell. C) Ragone plot comparing the NVOPF array//VO₂ NS hybrid device with other state-of-the-art reported energy storage systems.^[25–27] The energy and power densities are based on the total active material masses of cathode and anode. Solid circles represent Na-ion batteries: NVPF//MnFe₂O₄,^[28] VOPO₄//Na₂Ti₃O₇,^[27] NVP//Sb@TiO_{2-x},^[26] Na_{2/3}Ni_{1/3}Mn_{2/3}O₂//Sb,^[29] symmetric Na_{0.8}Ni_{0.4}Ti_{0.6}O₂,^[25] empty circles with solid line denote to Na-ion hybrid: Na₂Fe₂(SO₄)₃//Ti₂CT,^[30] AC//V₂O₅-CNT,^[31] empty circles with dotted line are Li-ion hybrid: AC//Nb₂O₅,^[32] AC//TiO₂@rGO.^[33]

that the charge storage mechanism for the GF-VO₂ NS electrode is capacitor-like over much of its operating range. The total capacity can be further quantified by separating the current response into diffusion-controlled and capacitive contributions.^[4,21] Figure S11B (Supporting Information) shows that some 76% of the total capacity is capacitive, even at a relatively slow sweep rate of 0.8 mV s⁻¹ when diffusion contributions are maximized. The specific capacity for the VO₂ NS electrode is much larger than what one expects for the double-layer capacitance from a conductive surface.^[22] These results suggest that the capacitive current is dominated by a pseudocapacitive process. From a morphology standpoint, it is likely that the fast kinetics and high fraction of capacitive current observed in this electrode system stem from the mesoporous and thin-sheet features of the VO₂.

The availability of the NVOPF positive electrode array and the VO₂ nanosheet negative electrode allow us to construct a full-cell device with the objective of achieving high-rate sodium

ion storage (see schematic in Figure 4A). A sodium ion storage device was assembled using two pieces of GF supported flexible electrodes (inset in Figure 4B). The device was operated under galvanostatic conditions at room temperature in a voltage window of 1 to 4 V. The discharge profiles in Figure 4B demonstrate two sloping stages suggesting a combination effect from both the intercalation cathode and pseudocapacitive anode. The hybrid device can be effectively discharged at rates from 1 to 20 C. It delivers a reversible capacity of ≈90 mA h g⁻¹ at 1 C and 48 mA h g⁻¹ at 12 C on the basis of mass from both anode and cathode active materials. The folded pouch cell shows identical electrochemical performance compared with the flat one (Figure S13A, Supporting Information), demonstrating its excellent mechanical flexibility and stability. To the best of our knowledge there are no other flexible sodium-ion batteries or sodium-ion hybrid energy storage devices that can deliver this level of high-rate capacity. Cycling studies carried out at a rate of 4 C indicate that about 80% of the capacity is retained after

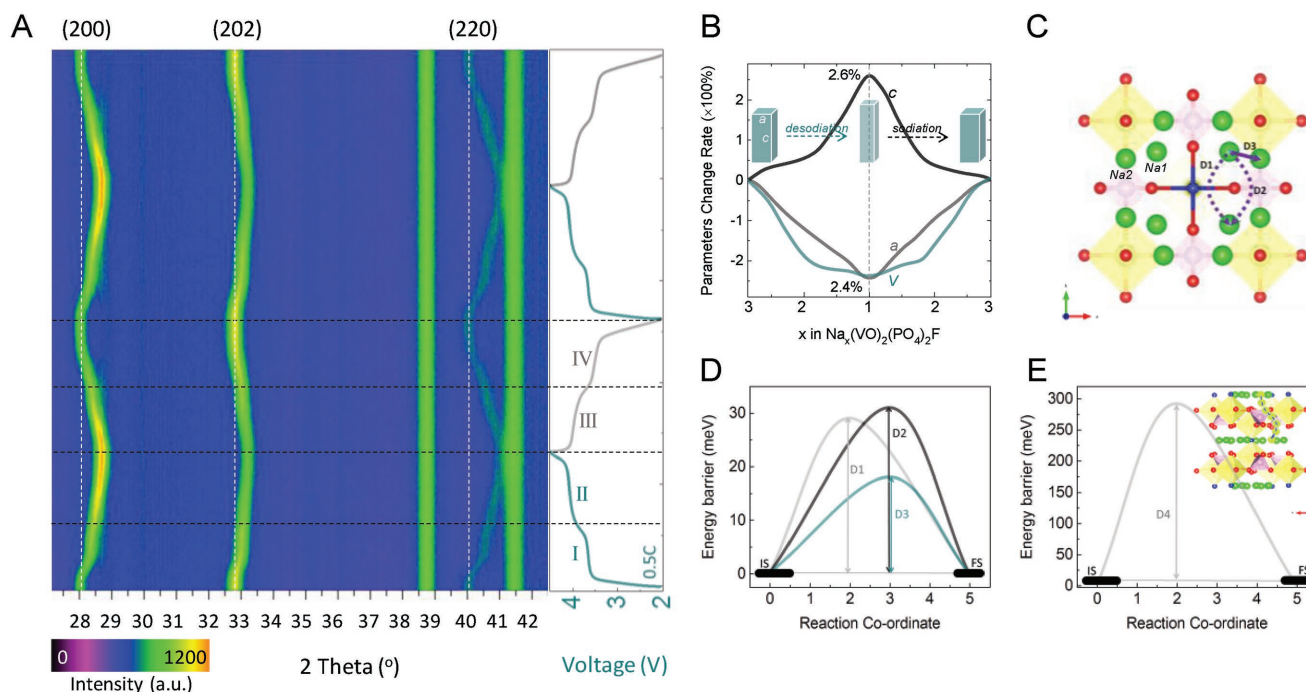


Figure 5. Electrochemical process analysis and mechanism of fast kinetics. A) In situ XRD contour plot collected during galvanostatic discharge/charge at 0.5 C of the NVOPF array electrode. B) Changes in lattice parameters a , c , and volume, V , during Na^+ deintercalation/intercalation. Inset: Illustration of the structure evolution. C, D) First-principle calculation of the in-plane (ab) diffusion pathways and the corresponding energy barriers for Na-ion migration. E) First-principles calculation of Na^+ migration barrier along c -direction. The arrows indicate optimum diffusion paths. IS: initial state; FS: final state.

220 cycles (Figure S13B, Supporting Information). The Ragone plot in Figure 4C compares the array-based NVOPF// VO_2 hybrid device with other reported Na-ion storage devices. Our device exhibits a maximum energy density of $\approx 215 \text{ W h kg}^{-1}$ (with power density 320 W kg^{-1}) and a maximum power density of 5200 W kg^{-1} (with energy density 60 W h kg^{-1}). More strikingly, the maximum energy density based on the mass of the whole electrode (including current collector) maintains at $\approx 170 \text{ W h kg}^{-1}$ thanks to the light-weight GF current collector and freestanding feature ($\approx 0.6 \text{ mg cm}^{-2}$ versus $\approx 10 \text{ mg cm}^{-2}$ for copper foil, and $\approx 15 \text{ mg cm}^{-2}$ for carbon cloth). This value corresponds to at least 100% increase in the energy density comparing with traditional copper foil incorporated electrodes. As summarized in Figure 4C and Figure S14 (Supporting Information), these characteristics are at least comparable to and probably slightly better than the best SIBs and Li^+/Na^+ ion hybrids reported to date.

We used in situ XRD to provide more insight about the structural changes of our 3D NVOPF array electrode during charge/discharge. Selected acquisition windows monitored the (200), (202), and (220) diffraction peaks during charge/discharge processes at 0.5 C (see Figure 5A and original XRD spectra in Figure S15, Supporting Information) and 1C (Figure S16, Supporting Information). It can be seen that the peaks shift to higher 2 theta angles during charging and return to their original positions in the subsequent discharge, suggesting that the process involves a solid solution reaction without any structure transition. The shift in peak positions is associated with the change in lattice parameters. A continuous decrease

in lattice parameter a occurs with sodium extraction; this process reverses during sodium insertion. The trend is opposite for lattice parameter c (see Figure 5B). The overall lattice volume shrinks when the first sodium is removed and remains relatively stable in the second Na removal, indicating that the structural change from $\text{Na}_3(\text{VO})_2(\text{PO}_4)_2\text{F}$ to $\text{Na}_2(\text{VO})_2(\text{PO}_4)_2\text{F}$ is larger than that from $\text{Na}_2(\text{VO})_2(\text{PO}_4)_2\text{F}$ to $\text{Na}(\text{VO})_2(\text{PO}_4)_2\text{F}$ upon Na ion deintercalation. The related total volume change is $\approx 2.4\%$ for the NVOPF array electrode, which is smaller than that of the NVOPF slurry electrodes ($\approx 2.9\%$, see Figure S17, Supporting Information) as well as other reported powder electrodes for SIBs, such as $\text{Na}_3\text{V}_2(\text{PO}_4)_3$ ($\approx 8.26\%$),^[34] $\text{Na}_3\text{V}_2\text{O}_2(\text{PO}_4)_2\text{F}$ ($\approx 2.79\%$),^[18] NaFePO_4 ($\approx 17\%$),^[35] $\text{Na}_2\text{FePO}_4\text{F}$ ($\approx 3.7\%$),^[36] NaFeSO_4F ($\approx 14.3\%$),^[37] and even LiFePO_4 ($\approx 6.8\%$) used in LIBs.^[37] This smaller lattice volume expansion may also be correlated with the orientation of individual arrays (Figure 2D) and help contribute to the long-term cycling stability.

The fast kinetics of the NVOPF array are consistent with the low Na^+ migration energy barriers determined from first principles calculations (Figure 5C–E). Figure 5C shows the calculated in-plane (ab) migration pathways D1, D2, and D3, where D3 from the Na1 site to a neighboring Na2 site exhibits the smallest energy barrier of 18 meV (Figure 5D). This value is much smaller than that of reported cathode materials for SIBs (Supporting Information).^[37] The energy barriers for in-plane Na^+ migration, including D1 (28 meV), D2 (< 31 meV), and D3 (18 meV) are all substantially less than that of perpendicular migration (292 meV) in Figure 5E, suggesting limited Na^+ transport in the c -direction and enhanced diffusion in (ab)

planes. These calculations provide a fundamental understanding for the experimental results in that the preferred orientation growth of the NVOPF along the (002) direction, which is perpendicular to the diffusion paths, is favorable for fast Na⁺ migration and the ability to support high rate energy storage.

In summary, a novel strategy has been developed to fabricate oriented arrays of Na₃(VO)₂(PO₄)₂F on flexible current collectors. These materials, which are based on the use of VO₂ nanosheets as seed layers, are capable of providing high-power as positive electrodes for SIBs. From in situ XRD experiments and first principles calculations, we can attribute the high rate properties of the NVOPF electrode to rapid ion transport within the *ab*-plane, the relatively low in-plane energy barrier and a small volume change upon the intercalation and deintercalation of sodium. A novel all-array Na⁺ hybrid energy storage device based on the NVOPF array cathode and a cogenetic pseudocapacitive VO₂ nanosheet anode is assembled for the first time, which was operated at rates up to 20 C and achieved energy densities as high as 215 W h kg⁻¹. These results establish that 3D array structures can serve as the basis for high-rate flexible Na ion energy storage devices.

Experimental Section

Synthesis and Characterization: 3D graphene foam was synthesized by chemical vapor deposition (First Nano's EasyTube 3000 System) from our previous methods.^[38] The 10 × 5 cm size Ni foams were used as scaffold templates with annealing flow of CH₄ (50 sccm), H₂ (100 sccm), and Ar (800 sccm) at 1000 °C for 2 min. Freestanding GF was obtained via etching of nickel template in a mixture solution of 0.5 M FeCl₃ and 0.1 M HCl. 3D VO₂ nanosheets were prepared by a facile solvothermal method. Hydrogen peroxide (0.5 mL, 30%) was added dropwise to vanadyl oxalate (2 mL, 6.6 × 10⁻³ M) in a 30 mL Teflon-lined stainless-steel autoclave. Then, 25 mL ethanol and one piece of substrate (carbon cloth or GF) was immersed into the solution. The autoclave was kept at 170 °C for 3 h. The resulting sample was collected by rinsing with deionized (DI) water and ethanol. Na₃(VO)₂(PO₄)₂F arrays were prepared using VO₂ NS as a seed layer precursor. In general, 8 mL aqueous solution was prepared at 90 °C with NH₄VO₃ (0.1 M), NH₄H₂PO₄ (0.1 M), NaF (0.05 M), Na₂CO₃ (0.05 M). The as-prepared VO₂ seed layer precursor was transferred into the autoclave with 8 mL of the solution and 20 mL *N,N*-dimethylformamide with adjusted PH value 6 by H₃PO₄. The system was sealed and heated at 180 °C for 6 h. The NVOPF particles were prepared by a similar method without immersing the VO₂ film during the solvothermal reaction. After washing with DI water and ethanol, the resulting product was coated by a thin layer of carbon by an annealing process in which an alumina boat with 1.5 mL ethylene glycol was loaded at the upstream zone of the quartz tube. The NVOPF array was obtained after maintaining the furnace at 400 °C for 20 min (mass loading of the NVOPF active material 3.1 mg cm⁻² and graphene foam 0.6 mg cm⁻²). The carbon annealing treatment was also applied to the VO₂ NS seed layer precursor in forming the VO₂ NS electrode (with active material mass loading 0.8 mg cm⁻²).

The various samples were identified using HRTEM (JEOL JEM-2010F at 200 kV). The XPS measurements were conducted by a VG ESCALAB 220i-XL system using a monochromatic Al Kα₁ source (1486.6 eV). Raman spectra were obtained with a WITec-CRM200 Raman system (WITec, Germany) with a laser wavelength of 532 nm (2.33 eV). Powder XRD collected on a PANalytical Empyrean diffractometer with Cu Kα radiation. For in situ XRD, measurements were made with a D8 DISCOVER X-ray diffractometer, using Cu Kα radiation ($\lambda = 1.5418 \text{ \AA}$) and a home-made electrochemical cell module with a beryllium window.^[39]

Electrochemical Measurements: Swagelok cells were assembled in an argon-filled glove box with the as-fabricated freestanding samples as the working electrode (without using binder or additives), metallic sodium

foil as the counter-electrode, 1 M NaClO₄ in ethylene carbonate—propylene carbonate—fluoroethylene carbonate (1:1:0.03 in volume) as the electrolyte, and a glass fiber separator. The NVOPF electrode that used particles (slurry electrode) was prepared by adding 10 wt% carbon black, and 5 wt% polyvinylidene fluoride dispersed in *N*-methyl-2-pyrrolidone, and dried at 120 °C under vacuum for 12 h before battery assembly. Galvanostatic charge/discharge, CV, and EIS measurements were carried out using Bio-logic potentiostat (VMP3). Long-term cycling was conducted on a LAND battery cycler (CT2001A). Prior to full cells fabrication, one cycle activation of VO₂ NS anode was performed. Full cells were assembled in a soft-packed pouch geometry using one piece of the GF-NVOPF array electrode as cathode and one piece of GF-VO₂ NS electrode as anode. The areal ratio between the anode and cathode freestanding film was 1:1.05. The energy and power densities were normalized to the total mass from both anode and cathode materials.

DFT Calculation: First-principles plane-wave calculations within DFT using projector-augmented wave potentials were performed using the Vienna ab initio simulation package. The exchange and correlation potentials were approximated by generalized gradient approximation. The Perdew–Burke–Ernzerhof exchange and correlation functional were considered. After energy convergence analysis, a plane-wave basis set with kinetic energy cutoff of 550 eV and Brillouin Zone sampling with Monkhorst Pack method of 4 × 4 × 4 k-points were chosen for the bulk phase calculations. All the parameters including the exchange and correlation functional and the E_{cut} are checked to make sure our calculation was creditable.

Supporting Information

Supporting Information is available from the Wiley Online Library or from the author.

Acknowledgements

D.L.C. and C.-H.L. contributed equally to this work. Z.X.S. acknowledges the financial support by the Ministry of Education, Singapore, Tier 1 (Grant No. M4011424.110) and Tier 2 (Grant No. M4020284.110). H.J.F. acknowledges the financial support by the MOE AcRF Tier 1 (RG12/17). The authors also acknowledge support from the Energy Research Institute @NTU (ERI@N). V.V.T.D.-N. acknowledges support from the University of California President's Postdoctoral Fellowship Program. C.-H.L. and B.D. acknowledge the support from the U.S. Office of Naval Research.

Conflict of Interest

The authors declare no conflict of interest.

Keywords

array electrodes, flexible batteries, Na-ion batteries, sodium vanadium fluorophosphates, sodium-ion capacitors

Received: January 7, 2018

Revised: January 23, 2018

Published online:

[1] J. W. Long, B. Dunn, D. R. Rolison, H. S. White, *Chem. Rev.* **2004**, *104*, 4463.

[2] M. R. Lukatskaya, B. Dunn, Y. Gogotsi, *Nat. Commun.* **2016**, *7*, 12647.

[3] Z. Chen, W. Ren, L. Gao, B. Liu, S. Pei, H. M. Cheng, *Nat. Mater.* **2011**, *10*, 424.

- [4] C. Wu, X. Lu, L. Peng, K. Xu, X. Peng, J. Huang, G. Yu, Y. Xie, *Nat. Commun.* **2013**, *4*, 2431.
- [5] X. Wang, X. Lu, B. Liu, D. Chen, Y. Tong, G. Shen, *Adv. Mater.* **2014**, *26*, 4763.
- [6] J. Meng, H. Guo, C. Niu, Y. Zhao, L. Xu, Q. Li, L. Mai, *Joule* **2017**, *1*, 522.
- [7] N. Li, Z. Chen, W. Ren, F. Li, H.-M. Cheng, *Proc. Natl. Acad. Sci. USA* **2012**, *109*, 17360.
- [8] X. H. Xia, D. L. Chao, Y. Q. Zhang, Z. X. Shen, H. J. Fan, *Nano Today* **2015**, *9*, 785.
- [9] Y. Xu, M. Zhou, Y. Lei, *Adv. Energy Mater.* **2016**, *6*, 1502514.
- [10] B. Liu, J. Zhang, X. Wang, G. Chen, D. Chen, C. Zhou, G. Shen, *Nano Lett.* **2012**, *12*, 3005.
- [11] J. Zhu, K. Sakaushi, G. Clavel, M. Shalom, M. Antonietti, T. P. Fellinger, *J. Am. Chem. Soc.* **2015**, *137*, 5480.
- [12] D. Chao, C. Zhu, P. Yang, X. Xia, J. Liu, J. Wang, X. Fan, S. V. Savilov, J. Lin, H. J. Fan, Z. X. Shen, *Nat. Commun.* **2016**, *7*, 12122.
- [13] V. L. Pushparaj, M. M. Shaijumon, A. Kumar, S. Murugesan, L. Ci, R. Vajtai, R. J. Linhardt, O. Nalamasu, P. M. Ajayan, *Proc. Natl. Acad. Sci. USA* **2007**, *104*, 13574.
- [14] H. Xia, Y. Wan, W. Assenmacher, W. Mader, G. Yuan, L. Lu, *NPG Asia Mater.* **2014**, *6*, e126.
- [15] D. Chao, P. Liang, Z. Chen, L. Bai, H. Shen, X. Liu, X. Xia, Y. Zhao, S. V. Savilov, J. Lin, Z. X. Shen, *ACS Nano* **2016**, *10*, 10211.
- [16] P. Zhang, L. Zhao, Q. An, Q. Wei, L. Zhou, X. Wei, J. Sheng, L. Mai, *Small* **2016**, *12*, 1082.
- [17] H. Jin, J. Dong, E. Uchaker, Q. Zhang, X. Zhou, S. Hou, J. Li, G. Cao, *J. Mater. Chem. A* **2015**, *3*, 17563.
- [18] M. Peng, B. Li, H. Yan, D. Zhang, X. Wang, D. Xia, G. Guo, *Angew Chem., Int. Ed. Engl.* **2015**, *54*, 6452.
- [19] Y. Qi, L. Mu, J. Zhao, Y. S. Hu, H. Liu, S. Dai, *Angew Chem., Int. Ed. Engl.* **2015**, *54*, 9911.
- [20] G. A. Muller, J. B. Cook, H. S. Kim, S. H. Tolbert, B. Dunn, *Nano Lett.* **2015**, *15*, 1911.
- [21] T. Brezesinski, J. Wang, S. H. Tolbert, B. Dunn, *Nat. Mater.* **2010**, *9*, 146.
- [22] J. Wang, J. Polleux, J. Lim, B. Dunn, *J. Phys. Chem. C* **2007**, *111*, 14925.
- [23] M. Xu, L. Wang, X. Zhao, J. Song, H. Xie, Y. Lu, J. B. Goodenough, *Phys. Chem. Chem. Phys.* **2013**, *15*, 13032.
- [24] J. Z. Guo, P. F. Wang, X. L. Wu, X. H. Zhang, Q. Yan, H. Chen, J. P. Zhang, Y. G. Guo, *Adv. Mater.* **2017**, *29*, 1701968.
- [25] S. H. Guo, H. J. Yu, P. Liu, Y. Ren, T. Zhang, M. W. Chen, M. Ishida, H. S. Zhou, *Energy Environ. Sci.* **2015**, *8*, 1237.
- [26] N. Wang, Z. Bai, Y. Qian, J. Yang, *Adv. Mater.* **2016**, *28*, 4126.
- [27] H. Li, L. Peng, Y. Zhu, D. Chen, X. Zhang, G. Yu, *Energy Environ. Sci.* **2016**, *9*, 3399.
- [28] Y. Liu, N. Zhang, C. Yu, L. Jiao, J. Chen, *Nano Lett.* **2016**, *16*, 3321.
- [29] L. Liang, Y. Xu, C. Wang, L. Wen, Y. Fang, Y. Mi, M. Zhou, H. Zhao, Y. Lei, *Energy Environ. Sci.* **2015**, *8*, 2954.
- [30] X. Wang, S. Kajiyama, H. Iinuma, E. Hosono, S. Oro, I. Moriguchi, M. Okubo, A. Yamada, *Nat. Commun.* **2015**, *6*, 6544.
- [31] Z. Chen, V. Augustyn, X. Jia, Q. Xiao, B. Dunn, Y. Lu, *ACS Nano* **2012**, *6*, 4319.
- [32] J. Come, V. Augustyn, J. W. Kim, P. Rozier, P. L. Taberna, P. Gogotsi, J. W. Long, B. Dunn, P. Simon, *J. Electrochem. Soc.* **2014**, *161*, A718.
- [33] H. Kim, M.-Y. Cho, M.-H. Kim, K.-Y. Park, H. Gwon, Y. Lee, K. C. Roh, K. Kang, *Adv. Energy Mater.* **2013**, *3*, 1500.
- [34] Z. Jian, W. Han, X. Lu, H. Yang, Y.-S. Hu, J. Zhou, Z. Zhou, J. Li, W. Chen, D. Chen, L. Chen, *Adv. Energy Mater.* **2013**, *3*, 156.
- [35] J. Lu, S. C. Chung, S.-i. Nishimura, A. Yamada, *Chem. Mater.* **2013**, *25*, 4557.
- [36] B. L. Ellis, W. R. Makahnouk, Y. Makimura, K. Toghill, L. F. Nazar, *Nat. Mater.* **2007**, *6*, 749.
- [37] R. Tripathi, S. M. Wood, M. S. Islam, L. F. Nazar, *Energy Environ. Sci.* **2013**, *6*, 2257.
- [38] D. Chao, X. Xia, J. Liu, Z. Fan, C. F. Ng, J. Lin, H. Zhang, Z. X. Shen, H. J. Fan, *Adv. Mater.* **2014**, *26*, 5794.
- [39] M. Yan, L. Zhao, K. Zhao, Q. Wei, Q. An, G. Zhang, X. Wei, W. Ren, L. Mai, *Adv. Funct. Mater.* **2016**, *26*, 6555.